Commun. Comput. Phys.
doi: 10.4208/cicp.261213.030614a

Vol. **16**, No. 5, pp. 1389-1418
November 2014

Feature-Scale Simulations of Particulate Slurry Flows in Chemical Mechanical Polishing by Smoothed Particle Hydrodynamics

Dong Wang[1], Sihong Shao[2,*], Changhao Yan[1], Wei Cai[3,1] and Xuan Zeng[1,*]

[1] *State Key Laboratory of ASIC and System, School of Microelectronics, Fudan University, Shanghai 201203, China.*
[2] *LMAM and School of Mathematical Sciences, Peking University, Beijing 100871, China.*
[3] *Department of Mathematics and Statistics, University of North Carolina at Charlotte, Charlotte, NC 28223, USA.*

Received 26 December 2013; Accepted (in revised version) 3 June 2014

Communicated by Ming-Chih Lai

Available online 2 September 2014

Abstract. In this paper, the mechanisms of material removal in chemical mechanical polishing (CMP) processes are investigated in detail by the smoothed particle hydrodynamics (SPH) method. The feature-scale behaviours of slurry flow, rough pad, wafer defects, moving solid boundaries, slurry-abrasive interactions, and abrasive collisions are modelled and simulated. Compared with previous work on CMP simulations, our simulations incorporate more realistic physical aspects of the CMP process, especially the effect of abrasive concentration in the slurry flows. The preliminary results on slurry flow in CMP provide microscopic insights on the experimental data of the relation between the removal rate and abrasive concentration and demonstrate that SPH is a suitable method for the research of CMP processes.

AMS subject classifications: 76M28, 74F10, 70E18, 35Q30

Key words: Chemical mechanical polishing, smoothed particle hydrodynamics, particulate flow, rough pad, wafer defects, abrasive concentration.

1 Introduction

Chemical mechanical polishing (CMP) is a key process widely used in semiconductor manufacturing industry to provide local and global planarity of silicon wafers [1]. As

*Corresponding author. *Email addresses:* sihong@math.pku.edu.cn (S. H. Shao), xzeng@fudan.edu.cn (X. Zeng)

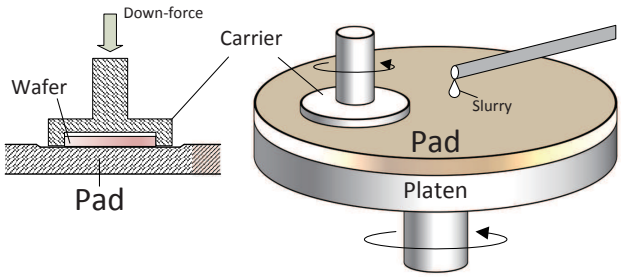

Figure 1: A sketch of the functional principle of chemical mechanical polishing (CMP). A wafer is mounted on the carrier and pressed upside-down against a polishing pad (the left plot). A chemical slurry with solid abrasives is deposited on the pad by the slurry delivery system. The rotation of both wafer and pad together with the chemical and mechanical effects of slurry leads to the planarization of wafer surface (the right plot).

illustrated in Fig. 1, during a CMP process, a wafer is mounted on a carrier and pressed upside-down against a polishing pad. A chemical slurry with solid abrasives sized from dozens of nanometres to several microns [1–5] is deposited on the pad by the slurry delivery system. The rotation of both wafer and pad together with the chemical and mechanical effects of slurry leads to the planarization of wafer surface. Although CMP has been extensively utilized in industry, the polishing mechanisms are still not well understood. This is due to the complex chemical and mechanical interactions at wafer-pad interface and the difficulties of in-situ observations at feature scales.

In CMP, the most important measurement is the material removal rate (MRR), which is determined by many factors, including chemical characteristics of the slurry, hydrodynamics of the slurry flow, the wafer-back pressure, the roughness and hardness of polishing pad, the rotation of wafer and pad etc. The commonly accepted description for MRR is based on Preston's theory [6] on glass polishing

$$\mathrm{MRR} = kPV, \tag{1.1}$$

where k is the coefficient of wafer-pad friction, P is the pressure applied on the wafer, V is the relative velocity between the wafer and the pad. A number of studies concerning various physical and chemical properties of the pad, the wafer and the slurry have been conducted to investigate the factors that influence the coefficient k. Among these chemical-mechanical factors, the hydrodynamics of the slurry flow attracts much attention. In recent years, numerous investigations with respect to the slurry hydrodynamics from wafer scale to feature scale have been carried out, including mathematical modellings [7–9], numerical simulations [10–12] and experimental studies [13–15]. The results of all these studies have indicated that the slurry plays an important role in material removals. For a comprehensive review of the research on slurry hydrodynamics, one can refer to [16] and references therein.

However, due to the complexity of the nano-structure and the topography at the pad-wafer interface, as shown in Fig. 2, it is difficult to directly probe the hydrodynamic phe-

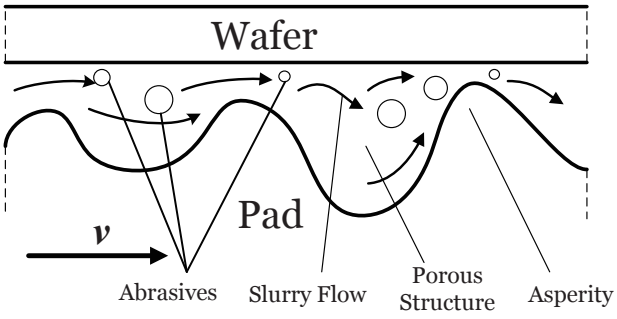

Figure 2: A sketch of the pad-wafer interface. The particulate thin slurry film is driven by the relative movement of the rough pad and the wafer.

nomena or develop a complete mathematical model. By contrast, computational fluid dynamics (CFD) simulation offers a much direct way to gain deep insight into the physics behind CMP. Runnels [10] was the very first to incorporate slurry flow into a feature scale CMP modelling. In his work, the slurry flow was bounded by a microscopic channel formed by a flat pad and a rough wafer with a feature; the slurry was assumed to be an incompressible Newtonian viscous fluid; the equation of motion was solved by a Galerkin finite element method; and an erosion rate V_n determined by the normal and shear stresses of the slurry was taken into account to formulate the MRR. Runnels' numerical results were in good agreement with the experimental data and indicated the importance of incorporating slurry effects into CMP modellings. After that, a series of CFD simulations taking account of various factors have been conducted, including the lubrication model [17], the evolution of wafer topography [11], the interface roughness [18], etc. These studies shed some light on the pressure distribution on the wafer, the estimation of material removal and the effect of surface roughness. However, because of the complexity and computational cost involved, only abrasive-free fluid simulations were carried out in all these studies.

Since the effects of solid abrasives are of great significance in CMP [5], it is necessary to incorporate these influences into a slurry simulation. A series of experimental investigations concerning the abrasive concentration were conducted by Bielmann et al. [2], Cooper et al. [19], Tamboli et al. [20] and Zhang et al. [21]. Although different materials were used in these studies, it was commonly reported that the MRR grows with the increase of abrasive concentration $wt\%$ and finally saturates when $wt\%$ reaches a threshold. Paul [22], Jeng et al. [23] and Wang et al. [24] tried to develop mathematical models concerning abrasive effects to predict MRR and got similar results with experiments. In all these work, no microscopic mechanisms were identified to explain the saturation of MRR in terms of abrasive concentration. This is the goal to be attempted in this paper. Currently, in the CMP research community, the simulation of feature scale abrasive effects is mostly conducted by molecular dynamics (MD) focusing on solid-solid inter-

actions [25–27], few investigations coupling abrasive motion and slurry hydrodynamics have been seen in the literature. Recently, Arbelaez et al. [12] tried to combine abrasives and slurry flow, but only for the case when the slurry flow was steady. The motion of the abrasives was caused by the stable fluid field. The influence of abrasives on the rheological characteristics of slurry flow were not taken into account.

In this work, a feature scale study will be carried out for an abrasive-filled particulate slurry flow with complex geometries, moving boundaries, fluid-solid interactions, and solid-solid collisions. In order to accurately deal with these complex conditions, an appropriate comprehensive CFD method is required, which will be developed in this paper. Among various CFD techniques, the Lagrangian mesh-free approaches are naturally suitable and widely used by the CFD community for this kind of problems. A competitive method in this framework is the smoothed particle hydrodynamics (SPH) method, developed independently by Lucy [28], Gingold and Monaghan [29] for astrophysical studies. Although SPH has been successfully utilized in a wide range of fluid dynamics problems [30], to the extent of our knowledge, there have been few SPH-based CMP slurry simulations. In the literature, we could find just a short paper [31] where only basic SPH formulations were used in studying the behaviour of slurry including polished debris.

The objective of the present work is to develop a SPH solver capable of simulating the CMP slurry containing as many realistic physical aspects as possible. Experimental results will be reconstructed by SPH simulations for the first time here. In order to achieve this goal, several numerical issues for the SPH method will be addressed. The first one is the modelling of moving rough pad and wafer. Here, a generalized dummy particle method suitable for arbitrarily shaped boundary developed by Adami et al. [32] is adopted. The second one is the handling of the motion of solid abrasives in the slurry. In the present paper, we successfully extended the aforementioned dummy particle approach to handle the floating objects in the slurry. Thus, a unified treatment for both solid boundaries and fluid-solid interactions is achieved, which significantly reduces the complexity of the SPH solver. Furthermore, to reduce computing cost, a novel efficient neighbour search algorithm [33] recently developed in our group is used.

The rest of the paper is organized as follows. In Section 2, the key technical issues of SPH proposed for CMP simulations are presented, including (a) the no-slip and no-penetration boundary treatments, (b) the suppression of tensile and density instabilities, (c) the slurry-abrasive interactions and (d) the solid-solid interactions. Then, the feature scale modelling issues of CMP, such as the pad asperity and non-contact models, are given in Section 3. In the numerical result section, Section 4, we first validate the proposed SPH method on simple flow problems with traditional CFD solvers. Then, we simulate the CMP process with Gaussian shaped rough pads and wafers containing features. Finally, we simulate the removal rate of slurry with abrasives and compare the results with experimental data. A good qualitative agreement is shown on the saturation of removal rate in terms of the abrasive concentration. The paper is concluded in Section 5 with a few remarks.

2 SPH for slurry flows

In this section, we first briefly present the basic formulations of SPH, and then modify them in several aspects so that the resulting SPH method is suitable for CMP slurry simulations. More details about SPH formulations and related numerical analysis can be found in [34].

2.1 SPH methodology

The basic principle of SPH is that any integrable function $A(\boldsymbol{r})$ can be expressed by an integral interpolation over the entire domain Ω as

$$A(\boldsymbol{r})=\int_{\Omega} A(\boldsymbol{r}')\delta(\boldsymbol{r}-\boldsymbol{r}')dV', \tag{2.1}$$

where $\boldsymbol{r}$ and $\boldsymbol{r}'$ are the position vectors, and $\delta(\boldsymbol{r}-\boldsymbol{r}')$ is the Dirac delta function. The key idea in SPH is to introduce a smooth kernel function $W(\boldsymbol{r}-\boldsymbol{r}',h)$ with compact support to approximate the Dirac delta function as follows

$$\int_{\Omega} W(\boldsymbol{r}-\boldsymbol{r}',h)d\boldsymbol{r}'=1, \quad \lim_{h\to 0} W(\boldsymbol{r}-\boldsymbol{r}',h)=\delta(\boldsymbol{r}-\boldsymbol{r}'), \tag{2.2}$$

where h is the so-called smoothing length which limits $W(\boldsymbol{r}-\boldsymbol{r}',h)$ in a compact support domain with radius $r_c=\kappa h$, i.e. $W(\boldsymbol{r}-\boldsymbol{r}',h)=0$ for $|\boldsymbol{r}-\boldsymbol{r}'|>r_c$, as shown in Fig. 3, and κ is a constant. There are many kinds of kernel functions [35] which usually take the following form

$$W(\boldsymbol{r}-\boldsymbol{r}',h)=\frac{1}{h^{\theta}}f(q), \tag{2.3}$$

where θ is the dimension of the system and $q=\frac{|\boldsymbol{r}-\boldsymbol{r}'|}{h}$. In this work, we employ a popular quintic spline kernel function [36] with $r_c=3h$

$$f(q)=\lambda\begin{cases}(3-q)^5-6(2-q)^5+15(1-q)^5, & 0\leqslant q<1,\\ (3-q)^5-6(2-q)^5, & 1\leqslant q<2,\\ (3-q)^5, & 2\leqslant q<3,\\ 0, & q\geqslant 3,\end{cases} \tag{2.4}$$

where λ is the normalization factor taking values $\frac{1}{120}$, $\frac{7}{478\pi}$, $\frac{3}{359\pi}$ in 1D, 2D, 3D spaces, respectively.

Replacing the Dirac delta function in Eq. (2.1) by $W(\boldsymbol{r}-\boldsymbol{r}',h)$, we obtain the basic SPH interpolation

$$A(\boldsymbol{r})=\int_{\Omega} A(\boldsymbol{r}')W(\boldsymbol{r}-\boldsymbol{r}',h)dV'. \tag{2.5}$$

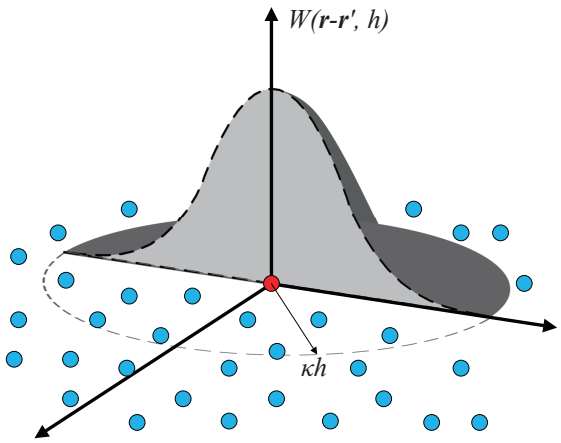

Figure 3: A sketch of the kernel function with compact support domain. The radius is $r_c=\kappa h$.

Using the summation over particles to approximate the integral, Eq. (2.5) becomes

$$A_i=\sum_j A_j W_{ij}\frac{m_j}{\rho_j}, \tag{2.6}$$

where the particle i has mass m_i, density ρ_i, position $\boldsymbol{r}_i$, $A_i=A(\boldsymbol{r}_i)$, $W_{ij}=W(\boldsymbol{r}_i-\boldsymbol{r}_j,h)$ and the summation is over all the particles but, in practice, it is only over near neighbours because $W(\boldsymbol{r}-\boldsymbol{r}',h)$ falls off rapidly with distance. Consequently, the derivative of $A(\boldsymbol{r})$ with respect to $\boldsymbol{r}$ at $\boldsymbol{r}_i$ can be given as [37]

$$\nabla A_i=-\sum_j A_{ij}\nabla_i W_{ij}\frac{m_j}{\rho_j}, \tag{2.7}$$

which is exact for a constant A, where $A_{ij}=A_i-A_j$ and ∇_i denotes the gradient with respect to the position of particle i. In the SPH community, the symmetric discretization of $\nabla A(\boldsymbol{r})$ is often used to overcome the poor performance of (2.7) in momentum calculation [38]. In this work, we adopted the particle-averaged spatial derivative proposed by Hu et al. [39]

$$\nabla A_i=\frac{1}{V_i}\sum_j (V_i^2+V_j^2)\tilde{A}_{ij}\nabla_i W_{ij}, \tag{2.8}$$

where $\tilde{A}_{ij}=\tilde{A}(A_i,A_j)$ is an inter-particle average value and $V_i=1/\sum_j W_{ij}$. This discretization conserves linear and angular momentum exactly. It should be noted that there are other kinds of discretizations in the literature, see e.g. [37, 40], and we choose here the discretization shown in (2.8) because it can be applied into multiphase flows [39] and easily combined with the dummy particle boundary condition proposed in [32], both of which are crucial in our CMP slurry simulations as discussed in Section 2.3.

2.2 Governing equations of SPH methods

The incompressible fluid can usually be approximated by a weakly compressible one [36, 41], of which the governing equations are given by the compressible isothermal Navier-Stokes equations

$$\frac{d\rho}{dt}=-\rho\nabla\cdot\boldsymbol{v}, \tag{2.9}$$

$$\rho\frac{d\boldsymbol{v}}{dt}=-\nabla p+\boldsymbol{\tau}+\rho\boldsymbol{f}, \tag{2.10}$$

where ρ is the fluid density, $\boldsymbol{v}$ is the velocity, p, $\boldsymbol{\tau}$ and $\boldsymbol{f}$ are the pressure, viscous force and body force, respectively. Eq. (2.9) is the well-known continuity equation and Eq. (2.10) is the momentum equation for the fluid. The pressure p in Eq. (2.10) is determined by the equation of state [42]

$$p=\frac{\rho_0 c^2}{\gamma}\left[\left(\frac{\rho}{\rho_0}\right)^{\gamma}-1\right], \tag{2.11}$$

where ρ_0 is the reference density which is often set equal to the initial density of fluid, c is the reference sound speed, and the exponent power γ is a constant. c is often set to 10 times reference velocity, i.e. the Mach number of the compressible flow is less than 0.1. The stiffness of the equation of state can be adjusted with the parameter γ and for fluids it is common to use $\gamma=7$. Assuming incompressibility of the fluid, the viscous force term in Eq. (2.10) can be simplified to

$$\boldsymbol{\tau}=\eta\nabla^2\boldsymbol{v}, \tag{2.12}$$

where η is the dynamic viscosity. Then, Eq. (2.10) turns into

$$\rho\frac{d\boldsymbol{v}}{dt}=-\nabla p+\eta\nabla^2\boldsymbol{v}+\rho\boldsymbol{f}. \tag{2.13}$$

Based on Eqs. (2.6), (2.7), and (2.8), one can derive a SPH discretization for (2.9) and (2.13) as follows [32]

$$\frac{d\rho_i}{dt}=\rho_i\sum_j\boldsymbol{v}_{ij}\cdot\nabla_i W_{ij}\frac{m_j}{\rho_j}, \tag{2.14}$$

$$\frac{d\boldsymbol{v}_i}{dt}=\frac{1}{m_i}\sum_j(V_i^2+V_j^2)\left(-\tilde{p}_{ij}\nabla_i W_{ij}+\tilde{\eta}_{ij}\frac{\boldsymbol{v}_{ij}}{r_{ij}}\frac{\partial W}{\partial r_{ij}}\right)+\boldsymbol{f}_i, \tag{2.15}$$

where $r_{ij}=|\boldsymbol{r}_{ij}|=|\boldsymbol{r}_i-\boldsymbol{r}_j|$ denotes the distance between particle i and j, $\frac{\partial W}{\partial r_{ij}}$ is the directional derivative in the direction of $\boldsymbol{e}_{ij}=\frac{\boldsymbol{r}_{ij}}{r_{ij}}$ (i.e. $\frac{\partial W}{\partial r_{ij}}=\nabla_i W_{ij}\cdot\boldsymbol{e}_{ij}$), $\tilde{p}_{ij}=\frac{p_i\rho_j+p_j\rho_i}{\rho_i+\rho_j}$ is the density-weighted inter-particle averaged pressure, and $\tilde{\eta}_{ij}=\frac{2\eta_i\eta_j}{\eta_i+\eta_j}$ is the inter-particle-averaged viscosity.

2.3 No-slip and no-penetration boundary treatments

For astrophysical problems where fluid moves in the absence of boundaries, imposing boundary condition was not a matter of a big concern in SPH. However, when applied to wall-bounded flows, SPH needs to address the important issue of enforcing suitable boundary conditions. Due to the absence of boundary terms in standard SPH formulations, the boundary conditions are usually imposed by adding boundary particles interacting with inner fluid particles.

In CMP, the fluid is driven by solid walls with complex topography. What makes the situation more complicated is the existence of floating rigid bodies (abrasives) in a slurry fluid. In order to simulate the interactions of these components with sufficient accuracy, we will utilize a dummy particle method developed by Adami et al. [32] in which several layers of fixed dummy particles are placed outside the boundary to provide full compact support for the fluid particles (see Fig. 4). To impose no-slip and no-penetration boundary conditions, the velocity and pressure of the border fluid particles are extrapolated to these dummy particles by

$$\boldsymbol{v}_d = 2\boldsymbol{V}_{wall} - \frac{\sum_f \boldsymbol{v}_f W_{df}}{\sum_f W_{df}}, \tag{2.16}$$

$$p_d = \frac{\sum_f p_f W_{df} + (\boldsymbol{f} - \boldsymbol{a}_{wall}) \cdot \sum_f \rho_f \boldsymbol{r}_{df} W_{df}}{\sum_f W_{df}}, \tag{2.17}$$

where d and f denote dummy particles and fluid particles, respectively, and $\boldsymbol{V}_{wall}$ is the prescribed wall velocity. The term concerning the influence of the body force $\boldsymbol{f}$ and the acceleration of solid wall $\boldsymbol{a}_{wall}$ in Eq. (2.17) is used to impose force balance at fluid-solid interface. Note that fluid-solid interactions are implemented directly by this method.

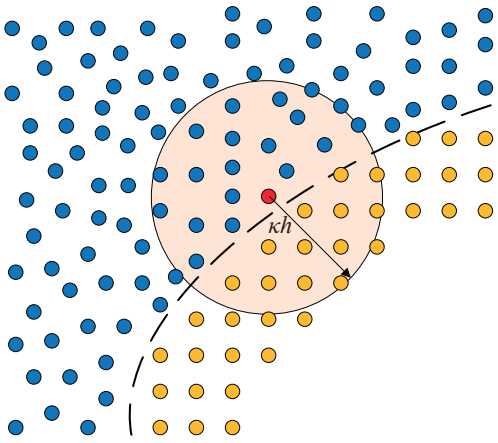

Figure 4: Full compact support for a given fluid particle (red) near the boundary by neighbouring fluid particles (blue) as well as dummy particles (orange).

Furthermore, since the dummy particles are fixed along the boundary, complex geometries can be handled easily. All these advantages make the dummy particle method the preferable choice for our work.

2.4 Tensile and density instability treatments of an improved SPH

In the weakly compressible fluid approach, the standard SPH scheme suffers from two main drawbacks. One is the well-known tensile instability caused by the clustering of negative-pressure fluid particles [43]. Various possible solutions have been proposed to eliminate such an instability. In this work, we employ a newly proposed method by Adami et al. [44], in which the movement of a particle is modified by an advection velocity $\tilde{\boldsymbol{v}}$ as

$$\frac{d\boldsymbol{r}_i}{dt}=\tilde{\boldsymbol{v}}_i, \tag{2.18}$$

$$\tilde{\boldsymbol{v}}_i(t+\Delta t)=\boldsymbol{v}_i(t)+\Delta t\left(\frac{\tilde{d}\boldsymbol{v}_i}{dt}-\frac{1}{\rho_i}\nabla p_b\right), \tag{2.19}$$

$$\frac{d\tilde{\boldsymbol{v}}_i}{dt}=\frac{d\boldsymbol{v}_i}{dt}+\frac{1}{m_i}\sum_j(V_i^2+V_j^2)\frac{\boldsymbol{A}_i+\boldsymbol{A}_j}{2}\cdot\nabla_i W_{ij}, \tag{2.20}$$

where p_b is the background pressure and $\frac{\tilde{d}\boldsymbol{v}_i}{dt}$ is the revised momentum equation by adding an advection tensor $\nabla\cdot\boldsymbol{A}$ with $\boldsymbol{A}=\rho\boldsymbol{v}(\tilde{\boldsymbol{v}}-\boldsymbol{v})$. It is shown in [44] that this technique significantly reduces the clumping of particles.

The other factor affecting the SPH simulation results is the occurrence of spurious oscillations in density and pressure fields. This phenomenon has not drawn much attention in the SPH community as the focus of most investigations is on the velocity field which can be simulated nicely [45]. But when the problem involves fluid-solid interaction, the pressure field becomes a critical issue. To solve this problem, we use a kernel gradient correction method [46] in which $\nabla_i W_{ij}$ in Eq. (2.14) is replaced by

$$\tilde{\nabla}_i W_{ij}=\boldsymbol{L}_i\nabla_i W_{ij}, \tag{2.21}$$

where $\boldsymbol{L}$ is the correction matrix defined as

$$\boldsymbol{L}_i=\left(-\sum_j V_j\nabla_i W_{ij}\otimes\boldsymbol{r}_{ij}\right)^{-1}. \tag{2.22}$$

With the help of this kernel gradient correction technique, the oscillations in density and pressure field can be reduced significantly.

2.5 Slurry flows in SPH modelling

In CMP process, the slurry is transported and delivered to the pad-wafer interface by the relative movement of the pad and the wafer. A thin film of slurry flow, with thickness

around 20 μm [47], is formed by pressing the wafer against the pad. Moreover, because of the existence of the asperities on pad surface, the gap between asperity tips and the wafer can be much thinner. At such a microscopic scale together with a comparably high velocity of the rough pad and the wafer, the slurry will behave quite differently from macroscopic bulk fluid. For example, higher shear rate in the thin slurry film can be observed at this scale [48].

In this work, the motion of slurry flow is calculated in the SPH framework. The fluid is driven either by the rough pad or by the plate wafer. On account of the Lagrangian characteristics, the fluid driven by the moving rough solid walls can easily be simulated. An important issue to be mentioned here is that the fluid is considered to be Newtonian, i.e. a constant viscosity for the fluid, despite of the fact that the fluid at this scale probably behaves as non-Newtonian. However, we note that SPH has been shown to be capable of handling non-Newtonian flows as well, see e.g. [49], which would be considered in our future work.

In the following, the modelling of two main physical processes in slurry flow will be discussed.

2.5.1 Slurry-abrasive interactions

One of the most difficult problems in CMP slurry modellings is the motion of floating abrasives (see Fig. 2), which makes the slurry a particulate fluid. Monaghan et al. [50] proposed a scheme describing the motion of the floating bodies by the solid wall boundary condition and Newton's law of motion. Satisfactory results have been obtained by similar approach, see e.g. [51]. In this work, in order to achieve a unified treatment for both solid boundaries and fluid-solid interactions, we extend the generalized dummy particle method described in Section 2.3, which has not been used so far to handle this kind of problem, to deal with floating bodies in slurry flows.

Let us consider one abrasive composed of many dummy particles in the SPH representation. The abrasive is regarded as rigid and surrounded by fluid particles, as illustrated in Fig. 5. The force applied on the dummy particle d from all its neighbouring fluid particles is

$$\boldsymbol{f}_d = m_d \sum_f \boldsymbol{f}_{df}, \tag{2.23}$$

where f denotes the fluid particle. The motion of a rigid abrasive S can then be written as

$$M_S \frac{d\boldsymbol{V}_S}{dt} = \sum_{d\in S} \boldsymbol{f}_d, \tag{2.24}$$

$$I_S \frac{d\boldsymbol{\Omega}_S}{dt} = \sum_{d\in S} (\boldsymbol{r}_d - \boldsymbol{r}_S) \times \boldsymbol{f}_d, \tag{2.25}$$

where M is the mass of the abrasive, I is the moment of inertia, $\boldsymbol{V}$ and $\boldsymbol{\Omega}$ are the velocity and angular velocity, respectively, and $\boldsymbol{r}_S$ is the centre of the rigid body. Finally, we have

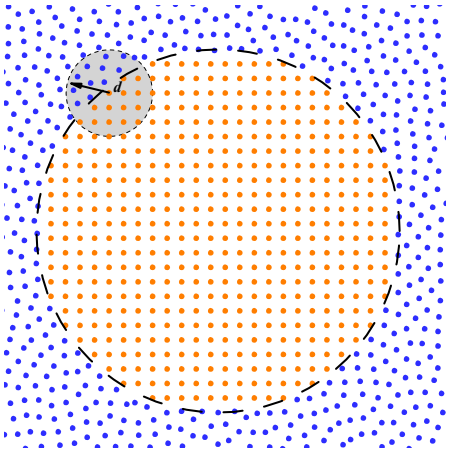

Figure 5: An abrasive is formed by dummy particles (orange). The force exerted on a dummy particle d is summed from all fluid particles (blue) in its support domain.

the motion equation of the dummy particles belonging to the rigid abrasive S

$$\frac{d\boldsymbol{r}_d}{dt}=\boldsymbol{V}_S+\boldsymbol{\Omega}_S\times(\boldsymbol{r}_d-\boldsymbol{r}_S). \tag{2.26}$$

2.5.2 Solid-solid repulsive interactions

Since there is no interactions between dummy particles in SPH, when the rigid bodies approach each other or a floating body moves close to the solid wall, no repelling will occur. This may lead to unphysical overlap of the solid materials. Therefore, it is necessary to introduce a repulsive force to avoid this phenomenon. Here, we take the form of the repulsive force proposed by Glowinski et al. [52]

$$\boldsymbol{F}_{ab}=\begin{cases}0, & |\boldsymbol{r}_{ab}|>R_a+R_b+\zeta,\\ \frac{c_{ab}}{\epsilon}\left(\frac{|\boldsymbol{r}_{ab}|-R_a-R_b-\zeta}{\zeta}\right)^2\frac{\boldsymbol{r}_{ab}}{|\boldsymbol{r}_{ab}|}, & |\boldsymbol{r}_{ab}|\leq R_a+R_b+\zeta,\end{cases} \tag{2.27}$$

where c_{ab} is the force scale, ϵ is the stiffness factor, $\boldsymbol{r}_{ab}$ is the position vector pointing from the centre of rigid body a to b, R is the radius of the rigid body, ζ is the penalty distance of the repulsive force. When the distance of two solid bodies is less than ζ, a strong repulsive force scaled by c_{ab} and ϵ will prevent them from penetrating each other. Meanwhile, if the floating abrasive approaches the solid wall, a mirror abrasive located outside the wall will be used to provide the repulsion

$$\boldsymbol{F}_{aw}=\begin{cases}0, & |\boldsymbol{r}_{aw}|>2R_a+\zeta,\\ \frac{c_{aw}}{\epsilon}\left(\frac{|\boldsymbol{r}_{aw}|-2R_a-\zeta}{\zeta}\right)^2\frac{\boldsymbol{r}_{aw}}{|\boldsymbol{r}_{aw}|}, & |\boldsymbol{r}_{aw}|\leq 2R_a+\zeta,\end{cases} \tag{2.28}$$

where $\boldsymbol{r}_{aw}$ is the position vector pointing from a to its mirror image.

2.6 Neighbour search algorithm

A large computational cost of SPH is associated with finding the neighbours of a given particle. Because of the compact support property of kernel function, only neighbour particles in the support domain need to be considered in the interpolation of A_i, which significantly reduces the computational costs of SPH. Thus, the development of an efficient neighbour search method is worthy of consideration.

A simple implementation of the neighbour search will traverse over all the particles. When the number of particles becomes very large, this method will be extremely time-costing. Therefore, many methods have been developed to reduce the search costs. Most of these applications are based on the grid-link-list algorithm [53] and the hierarchical tree structured algorithm [54]. Also, we have developed a competitive easy-to-parallelize neighbour search method [33] based on the plane-sweep algorithm, and implemented it in this work. Satisfactory speed-up has been achieved with the help of this new algorithm, which makes large-scale simulations possible. More details can be found in [33].

2.7 Time integration

Considering the advection correction method in velocity field to overcome tensile instability, a modified velocity-Verlet scheme [44] is used to perform the time integration

$$\boldsymbol{v}^{n+\frac{1}{2}} = \boldsymbol{v}^n + \frac{\Delta t}{2}\cdot\left(\frac{\tilde{d}\boldsymbol{v}}{dt}\right)^n, \tag{2.29}$$

$$\tilde{\boldsymbol{v}}^{n+\frac{1}{2}} = \boldsymbol{v}^{n+\frac{1}{2}} + \frac{\Delta t}{2}\boldsymbol{f}_{p_b}^n, \tag{2.30}$$

$$\boldsymbol{r}^{n+\frac{1}{2}} = \boldsymbol{r}^n + \frac{\Delta t}{2}\tilde{\boldsymbol{v}}^{n+\frac{1}{2}}, \tag{2.31}$$

where $\boldsymbol{f}_{p_b} = \frac{1}{\rho}\nabla p_b$ is the background pressure.

Then, the density is updated by Eq. (2.14) using the half time-step velocity $\boldsymbol{v}^{n+1/2}$ and position $\boldsymbol{r}^{n+1/2}$ as follows

$$\rho^{n+1} = \rho^n + \Delta t\left(\frac{d\rho}{dt}\right)^{n+\frac{1}{2}}. \tag{2.32}$$

Meanwhile, the position of the next step is updated by

$$\boldsymbol{r}^{n+1} = \boldsymbol{r}^{n+\frac{1}{2}} + \frac{\Delta t}{2}\tilde{\boldsymbol{v}}^{n+\frac{1}{2}}. \tag{2.33}$$

It should be noted that the advection velocity $\tilde{\boldsymbol{v}}$ is only used to move the particles to their new positions but not included in the calculation of density.

Finally, using the updated density ρ^{n+1} and position $\boldsymbol{r}^{n+1}$, the forces at step $n+1$ can be calculated. And the velocity for new time step can be obtained as

$$\boldsymbol{v}^{n+1} = \boldsymbol{v}^{n+\frac{1}{2}} + \frac{\Delta t}{2}\left(\frac{\tilde{d}\boldsymbol{v}}{dt}\right)^{n+1}. \tag{2.34}$$

If the advection correction for eliminating the tensile instability is not used here, i.e. ignoring the background pressure term $f_{p_b}^n$ in Eq. (2.30), the above time integration reduces to the conventional velocity-Verlet method.

The time step is set to the minimum of the Courant-Friedrichs-Lewy criterion [55], the viscous criterion [36] and the force criterion [56], namely,

$$\Delta t \leq \min\left(0.25\frac{h}{c}, 0.25\frac{h^2}{\nu}, 0.25\sqrt{\frac{h}{|f|}}\right), \tag{2.35}$$

where ν is the kinematic viscosity, f is the body force per mass on the particle.

In summary, the overall SPH algorithm for slurry flows with abrasives is given in Algorithm 1.

3 Feature scale modelling of CMP

The SPH method for slurry flows with abrasives developed in the last section will be used for feature scale CMP modelling next. Before presenting numerical results, in order to deal with feature scale CMP problems, several models of the CMP process will be established first.

3.1 Non-contact removal model

In the feature-scale CMP regime, there are two main models describing the mechanism of material removals. One is the contact model, where the pad directly contacts with the wafer. The abrasives in the slurry are indented into wafer surface and the materials on the wafer are scratched off the surface. This model is first introduced by Kaufman et al. [57] and later widely accepted in the CMP community, see e.g. [23]. However, it has been questioned recently and a new model based on the non-contact hypothesis (i.e. there is no real contact between pad and wafer) was proposed [58, 59]. Many experimental results have supported this hypothesis [60, 61]. In the non-contact model, the surface of the wafer is weakened by chemical reactions from the slurry. Then, only the surface molecules of the material are removed and carried away by the strong shearing force of the slurry and abrasives. In the present work, to investigate the effect of slurry flow in the entire domain, the pad and the wafer is completely separated by the slurry, i.e. the non-contact model is adopted.

3.2 Pad asperities

A typical polish pad is a polyurethane foam with great many porous structures. About 30-50% of the pad surface is covered by these porous structures with diameter 40-60 μm. Each pore is separated with wall structures (asperities) of width 10-50 μm [62]. From the

Algorithm 1 The skeleton of the SPH solver for slurry flows with abrasives.

Initialize and discretize the system into SPH particles.
for each time step $n=1,2,\cdots,N$ **do**
  for each fluid particle i **do**
    Update $\boldsymbol{v}^{n+\frac{1}{2}}$ by Eq. (2.29) using $(\frac{\tilde{d}\boldsymbol{v}}{dt})^n$
    Update $\tilde{\boldsymbol{v}}^{n+\frac{1}{2}}$ by Eq. (2.30) using background pressure $\boldsymbol{f}_{p_b}^n$
    Update $\boldsymbol{r}^{n+\frac{1}{2}}$ by Eq. (2.31) using $\tilde{\boldsymbol{v}}^{n+\frac{1}{2}}$
  end for
  for each rigid body S **do**
    Update $\frac{d\boldsymbol{V}_S}{dt}$ and $\frac{d\boldsymbol{\Omega}_S}{dt}$ by Eqs. (2.24) and (2.25) from dummy particles $d\in S$
    Update the velocity and position of dummy particles at $n+\frac{1}{2}$ by Eq. (2.26)
  end for
  Do neighbour searching
  Correct kernel gradient by Eqs. (2.21) and (2.22)
  Calculate $(\frac{d\rho}{dt})^{n+\frac{1}{2}}$ by Eq. (2.14) using $\boldsymbol{v}^{n+\frac{1}{2}}$ and $\boldsymbol{r}^{n+\frac{1}{2}}$ according to the neighbour list
  for each fluid particle i **do**
    Update ρ^{n+1} by Eq. (2.32)
    Update particle position $\boldsymbol{r}^{n+1}$ by Eq. (2.33) using $\tilde{v}^{n+\frac{1}{2}}$
  end for
  for each rigid body S **do**
    Update the position of dummy particles at $n+1$ by Eq. (2.26)
  end for
  Do neighbour search
  Extrapolate pressure, velocity of fluid field to dummy particles
  Correct kernel gradient by Eq. (2.21) and (2.22)
  Calculate the forces in Eq. (2.15) at $n+1$ using ρ^{n+1} and $\boldsymbol{r}^{n+1}$
  for each fluid particle i **do**
    Update velocity $\boldsymbol{v}^{n+1}$ using forces at $n+1$ by Eq. (2.34)
  end for
  for each rigid body S **do**
    Update $\frac{d\boldsymbol{V}_S}{dt}$ and $\frac{d\boldsymbol{\Omega}_S}{dt}$ by Eqs. (2.24) and (2.25) from dummy particles $d\in S$
    Update the velocity of dummy particles at $n+1$ by Eq. (2.26)
  end for
  Update Δt by Eq. (2.35)
end for

profile view of the pad-wafer interface at feature scale, as illustrated in Fig. 2, the pad asperity behaves like a brush sweeping along the surface of the wafer. The moving of these asperities significantly changes the hydrodynamics of slurry flows, leading to the effective removal of the materials. In this work, the pad surface is modelled by several layers of dummy particles which provide full compact support for the fluid particles near the boundary. These dummy particles do not only prevent fluid particles from penetrating the boundary, but also act as solid walls propelling fluid particles into motion.

Generally, the pad is elastic and deforms under the pressure from the wafer carrier. The modelling of pad usually incorporates elastic mechanics and contact mechanics theory. Although the elastic dynamics can be simulated very well in the SPH framework, see e.g. [63], the present work as the first step assumes the pad to be rigid, i.e. no deformations of the pad occur during the simulation, and all the dummy particles forming the pad are fixed to their relative positions.

4 Numerical results

In this section, we first validate the proposed SPH method for simple flows with traditional CFD solvers. Then, the CMP process with Gaussian shaped rough pads and wafers containing features are investigated by SPH. Finally, we calculate the removal rate of slurry with abrasives through SPH simulations.

4.1 Validation of the SPH solver

We will validate our SPH solver with traditional flow solvers in two cases.

4.1.1 Case 1 – shear flow in a rough-wall channel

In order to validate the model for a pad asperity, a SPH simulation of shear flow in a two-dimensional rough-boundary channel is conducted. As illustrated in Fig. 6, the channel consists of a plate as the top wall and a sine-shaped boundary as the bottom wall. The length of the channel is L and the height H can be expressed by

$$H = H_0 + H_A \cos\left(\frac{2\pi}{L}x\right). \tag{4.1}$$

The two walls are moving relatively to each other. As a result, the fluid is driven by the drag from the moving wall. The system is similar to, but slightly different from the unwrapped journal bearing model which often appears in thin film lubrication field [64]. For the journal bearing model, the curvature and the side leakage of fluid film can usually be neglected when $L \gg H$, thus the model can be reduced to a Reynold's equation, of which the analytical solutions are available [64]. However, in our case, the reduced Reynold's equation is not longer valid for L is comparable with H and we do not have analytical solutions any more.

Here, we let one of the two walls move while keep the other stationary. Both the motion of the top wall and the bottom wall are simulated. Due to the roughness of the bottom wall, it is difficult to conduct the simulation by mesh-based methods. However, for SPH, on account of its mesh-free characteristics, the code for simulating the movement of the bottom wall is almost identical to that for the top wall.

We set $L = 3\times10^{-5}$ m, $H_0 = 1\times10^{-5}$ m, $H_A = 5\times10^{-6}$ m, the density of fluid $\rho =$ 1000 kg/m^3, the dynamic viscosity $\eta = 1\times10^{-3}$ Pa·s. The moving wall has a horizontal

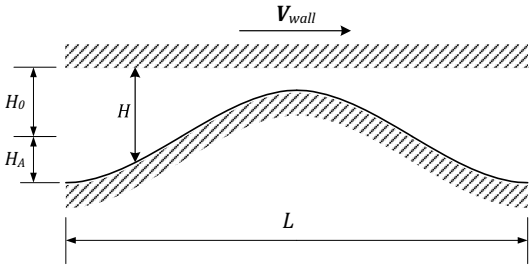

Figure 6: A sketch of the channel with sine-shaped boundary.

velocity $V_{wall}=1$ m/s. We set the sound speed $c=10V_{wall}$ to keep the Mach number less than 0.1. Periodic boundary conditions are implemented at the inlet and outlet of the channel. The dummy particle method is used to mimic the no-penetration solid wall and the no-slip boundary condition for the velocity and the Neumann boundary condition for the pressure are applied. The initial particle spacing Δx is 1×10^{-7} m, i.e. 30000 fluid particles are used.

We take the results calculated by the finite element method (provided by FLUENT, a commercial software) for the same system as the reference solutions. Fig. 7(a) compares the pressure on the top wall calculated by SPH (one simulation is moving the top wall, the other is moving the bottom wall) and FLUENT (only moving the top wall) at the instant when the stationary state is reached. In Fig. 7(b), the results of the shear stress on the top wall obtained by SPH and FLUENT are shown. The 2D plots of the pressure field in the entire channel for both SPH and FLUENT are shown in Fig. 8. From Figs. 7 and 8, we observe that the two SPH simulations give almost identical results and the results from SPH and FLUENT reach a satisfactory agreement. Moreover, moving the curved wall (the bottom wall in Fig. 6) causes much sharper change in the initial fluid field than

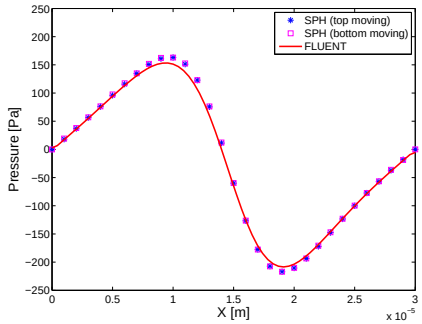

(a) Pressure.

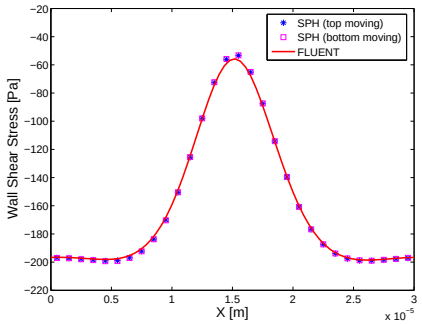

(b) Shear stress.

Figure 7: Comparison of the forces on the top wall calculated by SPH (one simulation is moving the top wall, the other is moving the bottom wall) and the commercial software FLUENT.

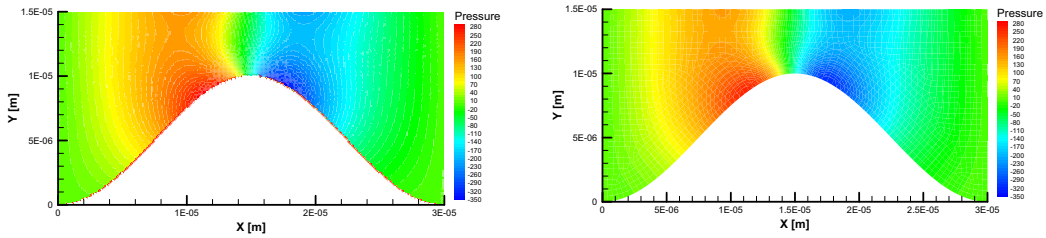

(a) SPH. (b) FLUENT.

Figure 8: Comparison of the pressure field obtained by SPH (a) and FLUENT (b).

moving the flat wall (the top wall in Fig. 6), so that the channel flow is more difficult to reach stationary state in the former case. An initial damping [41] is often introduced to solve such difficulty. In current simulations, we do not employ the initial damping, but still get satisfactory results. Actually, the time reaching the stationary state with SPH is 6×10^{-5} s (resp. 3×10^{-5} s) in the case of moving the curved (resp. flat) wall.

4.1.2 Case 2 – sedimentation of two cylinders in viscous fluid

To verify the model of fluid-solid interaction and solid-solid collision, we conducted a simulation of sedimentation of two cylinders in viscous flow. The two identical rigid cylinders are positioned along the central line of the vertical channel, as shown in Fig. 9(a). The system is initially at rest and the two cylinders will fall down due to gravity. The settling of the lower cylinder will generate a decrease in the pressure field behind, making the upper cylinder fall faster than the lower one. As a result, the upper cylinder will catch up with the lower one. Then, the two cylinders will form a binary body system, which usually rotates to make the centre line perpendicular to the stream in the viscous flow. Finally, the two cylinders separate. This phenomenon is well known as "drafting, kissing and tumbling" (DKT) [65], and has been numerically simulated in [52,66–68] with different numerical methods.

In this work, we adopt the same parameters in [52]. The channel width $L=0.02$ m, the height $H=0.06$ m. The diameter of the cylinder is 0.0025 m. The bottom left corner of the channel is set to be the origin, and the two cylinders are initially positioned at (0.01 m, 0.045 m) and (0.01 m, 0.05 m), respectively. The density of the fluid (resp. cylinder) is 1000 kg/m^3 (resp. 1500 kg/m^3). The dynamic viscosity of the fluid is 1×10^{-3} Pa·s. The system is discretized into particles with initial spacing $\Delta x=1\times10^{-4}$ m, namely, 124836 particles are used. To guarantee the accuracy of the weakly compressible flow approach, the sound speed c is set to be $10\sqrt{gH}$ with g being the gravitational acceleration. Each cylinder is formed by 484 latticed dummy particles. The motion of the cylinder is determined by the model of fluid-solid interaction discussed before in Section 2.5.1. The force scale factors c_{ab} and c_{aw} are of the same value as g and $\epsilon=5\times10^{-6}$. The penalty distance ζ in solid-solid collision shown in Eqs. (2.27) and (2.28) is $3\Delta x$.

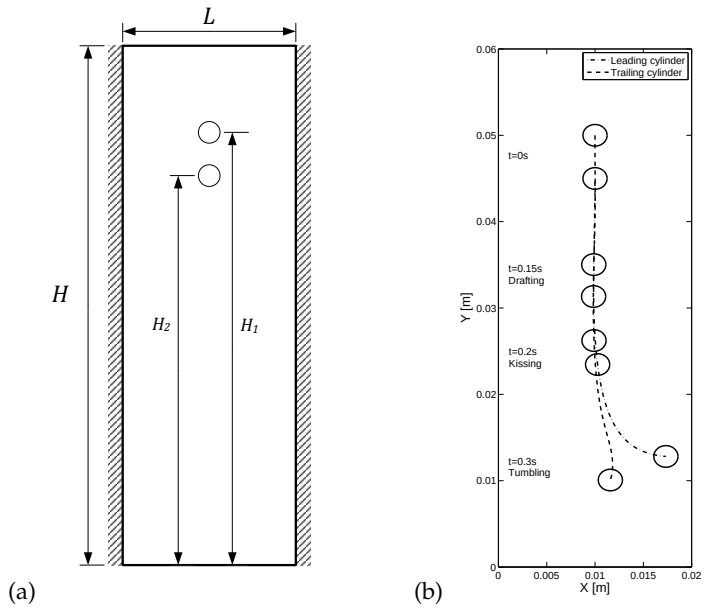

Figure 9: Sedimentation of two cylinders in a vertical channel: (a) The sketch of the system at initial state; (b) The snapshots of cylinder settling simulated by SPH, where the process of drafting ($t=0.15$ s), kissing ($t=0.2$ s) and tumbling ($t=0.3$ s) is clearly shown.

Fig. 9(b) shows the trajectories of the two cylinders in the SPH simulation and the DKT process is clearly observed. In Figs. 10 and 11, we further compare the horizontal position, the vertical position, the horizontal velocity and the vertical velocity calculated with SPH with those obtained by Glowinski et al. with a Lagrange-multiplier-based fictitious domain method [52] and by Uhlmann with an immersed boundary method [68]. It is shown there that the results from aforementioned two methods and SPH are in good agreement until the "kissing" stage starts. After the collision of two cylinders, the fluid field could be unstable and sensitive to the numerical methods adopted, as shown in Figs. 10 and 11. Such instability has been also reported before by Uhlmann [68], and our results are in more agreement with that by Uhlmann than by Glowinski et al. In a word, our SPH solver in Algorithm 1 can capture the physical moving trend of the two cylinders and thus is able to mimic the fluid-solid interactions and the solid-solid collisions existing in the CMP Slurry.

4.2 Flow with a Gaussian asperity and a flat wafer

In a previous work of our group [62], the effect of pad asperities on material removal in CMP was modelled and the importance of pad-wafer geometries was discussed in detail. However, the slurry flows were not included in that work. To further understand the geometrical effect on slurry hydrodynamics, we conducted a series of simulations using a moving wall with a Gaussian shape. As illustrated in Fig. 12(a), the channel consists of

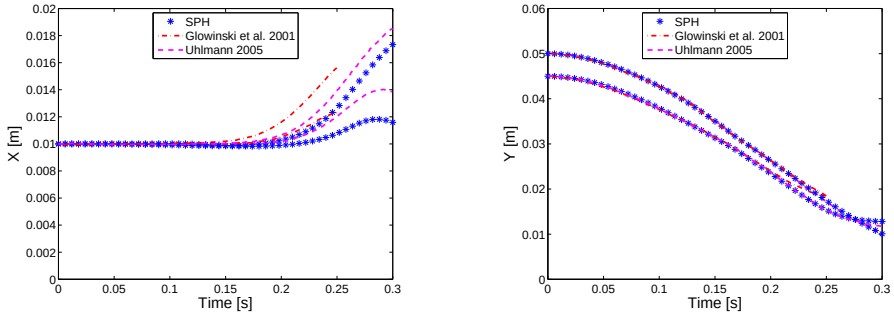

(a) Horizontal position. (b) Vertical position.

Figure 10: Comparison of the position of the two cylinders calculated in this paper with SPH, by Glowinski et al. [52] and by Uhlmann [68].

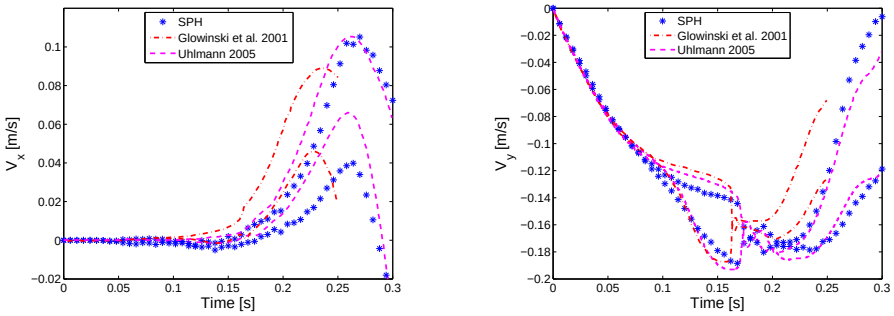

(a) Horizontal velocity. (b) Vertical velocity.

Figure 11: Comparison of the velocity of the two cylinders calculated in this paper with SPH, by Glowinski et al. [52] and by Uhlmann [68].

a plate and a Gaussian-curve wall (asperity), of which the height is defined by

$$H=(H_{max}-H_{gap})e^{-\frac{(x-x_0)^2}{2\sigma^2}}, \tag{4.2}$$

where x_0 denotes the position of the peak and σ determines the width of the rough boundary. The curved wall is used to mimic the pad asperity and the plate represents the wafer surface. The fluid is moved by the curved wall at a velocity V_{wall} in horizontal direction, which is very similar to the CMP process.

The system is set in accordance with the genuine CMP materials. The fluid film thickness is around 2×10^{-5} m [18, 47], and the width of asperity is from 1×10^{-6} m to 1×10^{-5} m, and σ from 2×10^{-6} m to 1×10^{-5} m. The velocity of the moving boundary is $V_{wall}=1$ m/s and the largest gap between the two boundaries is $H_{max}=2\times10^{-5}$ m. The fluid is set as water with $\rho=1000$ kg/m^3 and $\eta=1\times10^{-3}$ Pa·s. The initial particle spacing $\Delta x=2\times10^{-7}$ m. The sound speed is set to be $10V_{wall}$.

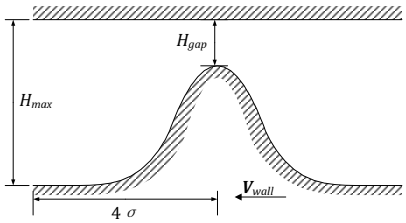

(a) Flat wafer.

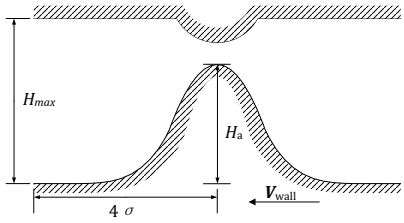

(b) Arc-shaped feature.

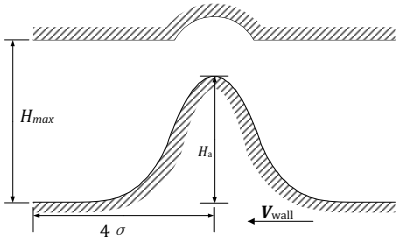

(c) Cavity.

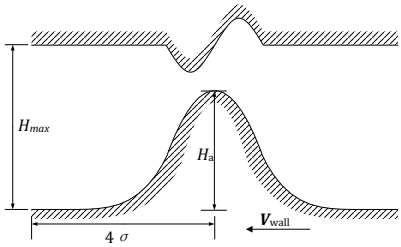

(d) Sine-shaped feature.

Figure 12: Sketches of the channel with a Gaussian-curve asperity on the bottom wall and several types of typical features on the top wall.

The effects of σ and H_{gap} on the maximum fluid pressure along the horizontal line $y = H_{max}$ are shown in Fig. 13, from which we can see that the pressure increases almost linearly with the increment of the width of the asperity (see Fig. 13(a) and e.g. the slope is about 9.28 for $H_{gap} = 7\times10^{-6}$ m), but grows exponentially when the gap becomes narrow (see Fig. 13(b) and e.g. the curve is $e^{-3.636H_{gap}}$ for $\sigma = 6\times10^{-6}$ m). Therefore, it can be concluded that the height of the asperity plays a more important role in influencing the fluid pressure distribution.

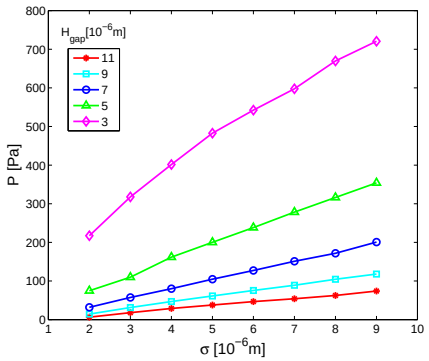

(a) Effect of asperity width σ.

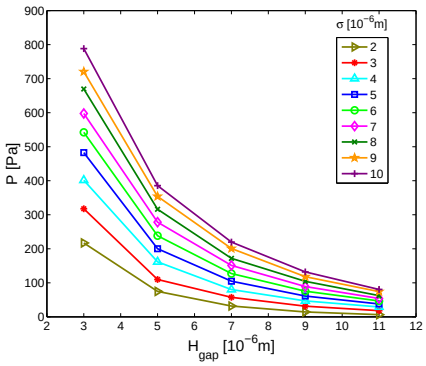

(b) Effect of asperity height H_{gap}.

Figure 13: Effect of the asperity geometry on the pressure.

4.3 Flow with a Gaussian asperity and a wafer with features

When the wafer surface is not flat, the pressure distribution will change by the features of the wafer. High pressure zone would occur in the feature area of the wafer and lead to a large material removal rate. Simulations on the effect of wafer features on the fluid have been reported by Qin [69] using a finite element method. His results indicated that the removal of materials will start in the corner first and then happen on the bulk of the feature. However, Qin only considered the planar pad surface and the flow was driven by the motion of the flat pad. In our simulations, we investigate the effect of both pad asperities and wafer features on the fluid. Particularly, three cases with different wafer topography are conducted below.

4.3.1 Case I – Arc-shaped feature on the wafer

As illustrated in Fig. 12(b), the channel consists of two rough solid boundaries. The top boundary mimics the wafer with an arc-shaped feature, while the bottom surface defined by Eq. (4.3) is used to simulate a rough pad

$$H = H_a e^{-\frac{(x-x_0)^2}{2\sigma^2}}. \tag{4.3}$$

Here, we set the channel length $L = 8\sigma$ with $\sigma = 5\times10^{-6}$ m, the height of the asperity $H_a = 1.3\times10^{-5}$ m, and the largest gap of the channel $H_{max} = 2\times10^{-5}$ m. The radius of the arc feature on the top boundary is 5×10^{-6} m. The central angle of the arc is $2\pi/3$ in radian, making the height of the feature 2.5×10^{-6} m.

To simulate the polishing process, we move the bottom wall horizontally and periodically at a constant speed of $V_{wall} = 1$ m/s. Thus the period T of the movement of asperity is 4×10^{-5} s. The density of the fluid $\rho = 1000$ kg/m^3 and the dynamical viscosity $\eta = 1\times10^{-3}$ Pa·s. The initial particle spacing $\Delta x = 2\times10^{-7}$ m and the sound speed is set to

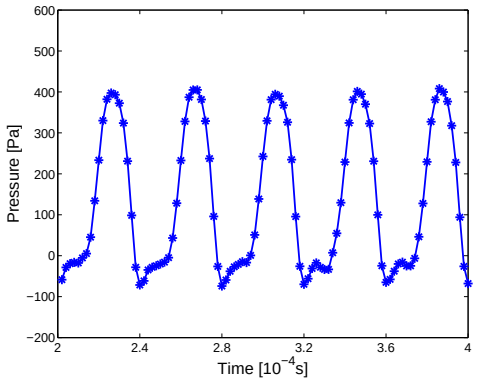

Figure 14: Evolution of the pressure at the sample point (2.3×10^{-6} m, 1.85×10^{-6} m) located at the feature surface. The largest pressure occurs at about $0.7T$.

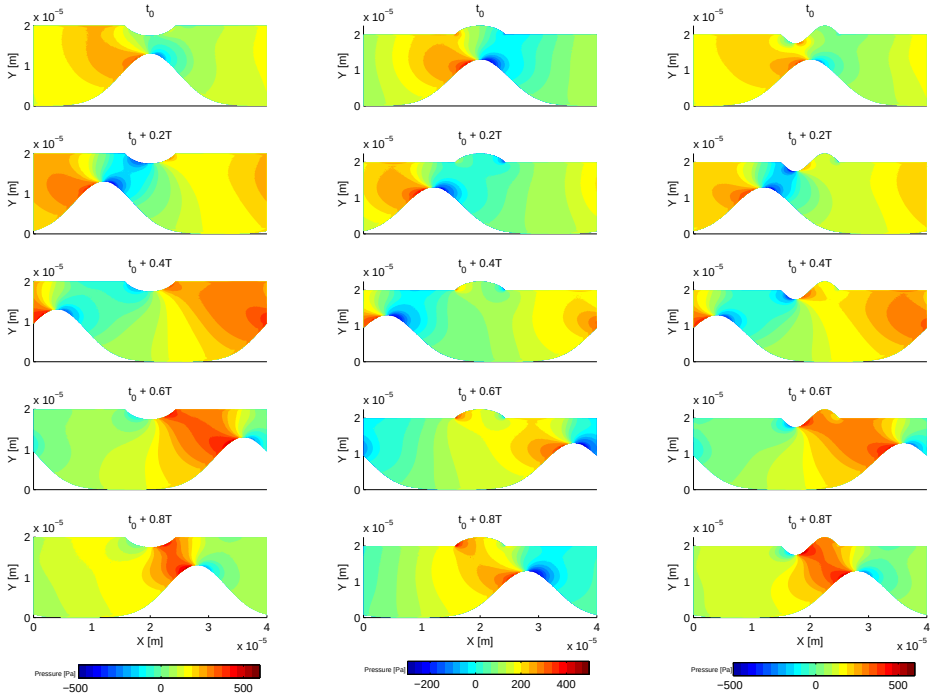

(a) Arc-shaped feature. (b) Cavity on the wafer. (c) Sine-shaped defect.

Figure 15: Evolution of the pressure field of flows with a Gaussian asperity and a wafer with different features at different time instants.

be $10V_{wall}$. The evolution of the pressure field at different instants is shown in Fig. 15(a), from which we can observe that: (a) A high pressure zone (red) appears around the tip of the asperity; (b) When the asperity is getting close to the feature, the high-pressure zone extends to the corner area of the feature. Finally, the pressure on the feature reaches its peak value at about $0.7T$ (see Fig. 14).

It is widely accepted that the removal happens when the forces on the wafer surface grow over the bond-break threshold of surface molecules and the MRR is sensible to the magnitude and frequency of the stresses on the wafer [58,60,61]. From the results shown in Figs. 14 and 15, we could get a clear view of how the forces on the wafer accumulates. Meanwhile, the importance of pad asperity to the periodical force accumulation is manifested in this study.

4.3.2 Case II – A cavity on the wafer

In Case II, a hollow on the wafer (see Fig. 12(c)) is used to mimic the dishing of metal or erosion of dielectric in CMP. The parameters used in this case are the same as Case I except that the arc is turned upside down. Fig. 15(b) shows the evolution of pressure field

from t_0 to $t_0+0.8T$. Similar to Case I, a high pressure zone is formed around the corner area. This indicates that the removal will most probably happen near the corner, which agrees with the experimental results reported by White et al. [70]. In an electron microscopic image, it is shown clearly that a large removal occurs on the edge of a cylindrical polydimethylsiloxane post in a cylindrical well.

4.3.3 Case III – Sine-shaped feature on the wafer

The schematic of the Case III is plotted in Fig. 12(d). A sine-like defect is used in this case to mimic the topography of wafer surface due to the deposition of removed material behind the hollow. The deposing phenomenon is due to the abrasive-wafer collision and has been reported in many microscopic simulations, see e.g. [25,71]. The amplitude of the sine-like defect is 2.5×10^{-6} m in accordance with the height of arc features in Cases I and II, while other parameters keep unchanged. In Fig. 15(c), as expected, a high-pressure zone is formed around the pile when the asperity is approaching. With the help of the high stresses, the pile of weakened molecules behind the hollow can easily be transported away by slurry flows.

The results of the above three cases give us a preliminary insight of how the asperity-driving flow acts on the removal of materials. Near the area where material removal on the wafer most probably happens, a high-stress zone in the fluid field can be found. This phenomenon agrees well with the model in non-contact hypothesis, where the removal and advection of weakened materials are most conducted by the slurry flow. Since these critical behaviours of the slurry flow is influenced by the moving pad asperities, it can be demonstrated that the pad asperity plays an fundamentally important role in CMP process.

4.4 Effect of abrasives in the slurry flow

In order to investigate the behaviour of slurry including abrasives, several floating solid spheres represented by dummy particles are placed into the fluid as shown in Fig. 16. The channel consists of an infinite long plate and a periodical Gaussian-curve shaped

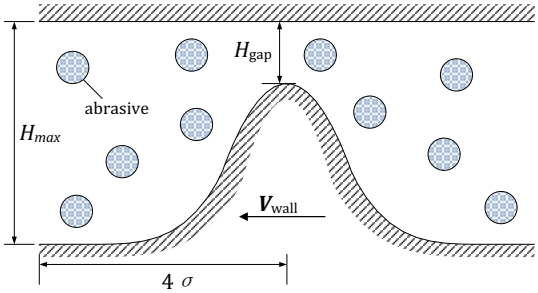

Figure 16: A feature-scale channel with a Gaussian-curve shaped wall and abrasives floating in the slurry.

Table 1: The relation between the abrasive concentration and the number of abrasives.

# of abrasives	4	8	11	15	19	22	25	29
$wt(\%)$	1.07	1.87	2.94	3.75	5.08	5.89	6.69	7.49

rough wall, and the fluid film thickness is determined by Eq. (4.2). In this simulation, we set $H=2\times10^{-5}$ m, $\sigma=5\times10^{-6}$ m, $V_{wall}=1$ m/s, $\rho=1000$ kg/m^3, $\eta=1\times10^{-3}$ Pa·s. The initial SPH particle spacing is 1×10^{-7} m. The diameter of each cylinder is 1×10^{-6} m, i.e. 80 dummy particles are used to form the sphere. The density of the abrasive is set to be 2000 kg/m^3. We performed a series of simulations with different abrasive concentration $wt\%$ from 1.07% to 7.49% for which the numbers of abrasives are calculated by

$$n=\frac{wt\%\rho_{fluid}V_{fluid}}{(1-wt\%)\rho_{abrasive}V_{abrasive}}. \tag{4.4}$$

All the cases we considered are listed in Table 1.

We found that when the abrasives were moving in the bulk area of the channel, only slight fluctuations in the pressure and wall shear on the top plate occurred. However, as shown from Fig. 18, when the abrasives were passing through the narrow gap (see Fig. 17), large variation of the pressure and wall shear can be observed.

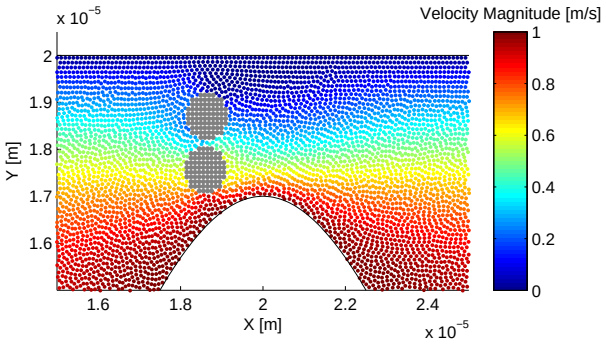

Figure 17: Fluid velocity field when solid abrasives passing through the narrow gap. The abrasives significantly change the thickness of fluid film, leading to large variation of stresses in gap area.

The effect of the abrasive concentration has been discussed widely in literature, see e.g. [5, 19, 20, 24, 72]. On one hand, experimental results show that MRR is proportional to $wt\%^{1/3}$ [19], and with the increase of $wt\%$, MRR will finally reach a saturation. On the other hand, it is broadly accepted that the MRR is proportional to the shear frequency F_τ of the solid abrasives [59–61]

$$\text{MRR}\propto F_\tau. \tag{4.5}$$

Since at feature scale, it is difficult to conduct in-situ measurement to verify the relationship between MRR and F_τ, a natural question can be asked: is there a relation between

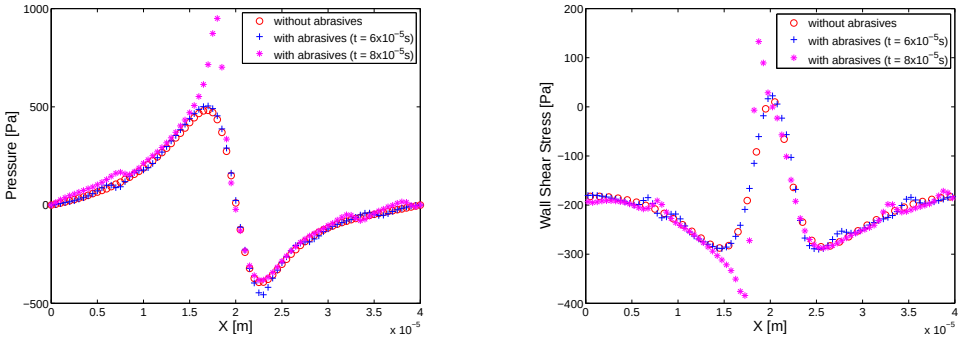

(a) Pressure. (b) Shear stress.

Figure 18: The forces on the top wall of abrasive-free case (red circle), abrasive-in-gap case (magenta *) and abrasive-beyond-gap case (blue +).

$wt\%$ and F_τ? or does $F_\tau \propto (wt\%)^{1/3}$ hold? We tried to answer this question with our SPH simulations.

From Fig. 18(b), large shear stress can be found when the abrasives passing through the wafer-pad gap. Since the shearing force τ plays an important role in material removing at feature scale [61], we assume that the material removal will most probably happen when the abrasive-leading high shear stress passes over a certain threshold τ_{th}. In this work, we set τ_{th} naturally to be the maximum shear stress on wafer surface when $wt\%=0$ (i.e. the abrasive-free case). With current settings, $\tau_{th}=288.5$ Pa. If $\tau \geqslant \tau_{th}$, then τ is considered as an *active shear*. Thus we could record the time t_{active} when the active shear occurs during a period of time t_{total} for various $wt\%$. In consequence, the frequency of the active shear is measured by

$$F_\tau = \frac{t_{active}}{t_{total}}. \tag{4.6}$$

Fig. 19 shows the relationship between the normalized abrasive concentration (by the maximum $wt\% = 7.49\%$ in Table 1) and the above shear frequency. We observed there that: (a) The shear frequency increases evidently as the number of the abrasives is increasing; (b) After a certain $wt\%$ (about 5%), F_τ reaches its saturation point and will not increase thereafter; (c) Before the saturation, we may have the relation $F_\tau \propto (wt\%)^{1/3}$ holds. Therefore, our results are in good agreement with the aforementioned experimental observation of the removal saturation in terms of abrasive concentration. Moreover, we confirmed numerically that $F_\tau \propto (wt\%)^{1/3}$ (which has not been done before either numerically or experimentally) holds before the saturation. It should be pointed out that since the establishment of threshold shear is based on the abrasive-free case, the analysis of active shear in this work can be applied to more complex and general situations in a straight way.

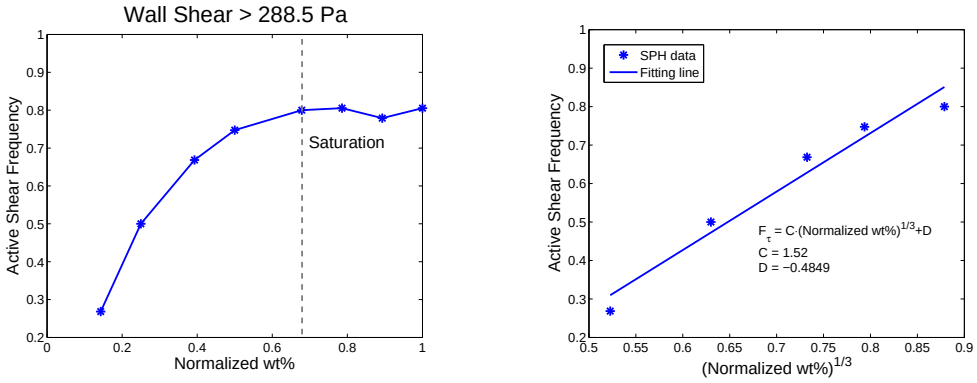

(a) (b)

Figure 19: The shear frequency v.s. the normalized abrasive concentration (by the maximum $wt\%=7.49\%$ in Table 1). (a) Shear frequency as a function of normalized $wt\%$. The grey dashed line denotes $wt\%=5\%$ (i.e. the normalized abrasive concentration is about 0.67). (b) Shear frequency as a function of (normalized $wt\%)^{1/3}$ before the saturation.

5 Conclusions

In this work, a systematic development of a SPH method is conducted, and the resulting SPH solver is suitable for the simulation of abrasive-filled slurry flow and rough pads and feature-scale wafers in a CMP process. The effects of rough pad, wafer defects, moving solid boundaries, slurry-abrasive interactions and abrasive collisions are taken into account by the developed SPH method.

Several recent improvements on SPH are integrated into the SPH method to yield better accuracy of fluid field. The methods for simulating solid floating and solid-solid collisions is coupled with SPH to simulate particulate slurry flow. Numerical validations show that SPH is able to capture the phenomena of the multi-physical aspects behind CMP.

The simulations of moving rough pad, geometry of several types of typical features on the wafer shed some light on the mechanisms of material removal in CMP. A thorough simulation concerning the abrasive concentration is carried out. The results of shear frequency based on statistical hypothesis are in a satisfactory qualitative agreement with the experimental data and demonstrate that SPH is a suitable method for studying complex CMP mechanisms.

This work, to some extent, can be further improved on several physical aspects. The non-Newtonian characteristics of slurry flow, the elastic properties of polishing pad, direct simulation of the interactions between the abrasives and the wafer are not taken into consideration in this paper. These issues together with the coupling of SPH and other computational methods, such as molecular dynamics for a deeper insight into the mechanisms of chemical mechanical polishing, will be the subject of our research in the future.

Acknowledgments

D.W., C.Y. and X.Z. were partially supported by National Natural Science Foundation of China (Nos. 61125401, 61376040, 61228401, 61274032), the National Basic Research Program of China (No. 2011CB309701), the National Major Science and Technology Special Project of China (Nos. 2011ZX01035-001-001-003, 2014ZX02301002-002), Shanghai Science and Technology Committee project (No. 13XD1401100) and the State Key Laboratory of ASIC and System (Fudan University) research project (No. 11MS013). S.S. was partially supported by the National Natural Science Foundation of China (Nos. 11101011, 91330110), the Specialized Research Fund for the Doctoral Program of Higher Education (No. 20110001120112) and the State Key Laboratory of ASIC and System (Fudan University) open research project (No. 10KF015). W.C. was partially supported by the US Army Office of Research (No. W911NF-11-1-0364), the National Science Foundation of USA (No. DMS-1315128) and the National Natural Science Foundation of China (No. 91330110).

References

[1] P. B. Zantye, A. Kumar, A. K. Sikder, Chemical mechanical planarization for microelectronics applications, Mat. Sci. Eng. R 45 (2004) 89–220.
[2] M. Bielmann, U. Mahajan, R. K. Singh, Effect of particle size during tungsten chemical mechanical polishing, Electrochem. Solid State Lett. 2 (8) (1999) 401–403.
[3] G. B. Basim, J. J. Adler, U. Mahajan, R. K. Singh, B. M. Moudgil, Effect of particle size of chemical mechanical polishing slurries for enhanced polishing with minimal defects, J. Electrochem. Soc. 147 (9) (2000) 3523–3528.
[4] C. Zhou, L. Shan, J. R. Hight, S. Danyluk, S. H. Ng, A. J. Paszkowskic, Influence of colloidal abrasive size on material removal rate and surface finish in SiO_2 chemical mechanical polishing, Tribol. Trans. 45 (2) (2002) 232–238.
[5] E. Matijević, S. V. Babu, Colloid aspects of chemical-mechanical planarization, J. Colloid Interface Sci. 320 (2008) 219–237.
[6] F. W. Preston, The theory and design of plate glass polishing machines, J. Soc. Glass Technol. 11 (1927) 214–257.
[7] S. R. Runnels, L. M. Eyman, Tribology analysis of chemical-mechanical polishing, J. Electrochem. Soc. 141 (6) (1994) 1698–1701.
[8] J. Tichy, J. A. Levert, L. Shan, S. Danyluk, Contact mechanics and lubrication hydrodynamics of chemical mechanical polishing, J. Electrochem. Soc. 146 (4) (1999) 1523–1528.
[9] S. Sundararajan, D. G. Thakurta, D. W. Schwendeman, S. P. Murarka, W. N. Gill, Two-dimensional wafer-scale chemical mechanical planarization models based on lubrication theory and mass transport, J. Electrochem. Soc. 146 (2) (1999) 761–766.
[10] S. R. Runnels, Freature-scale fluid-based erosion modeling for chemical-mechanical polishing, J. Electrochem. Soc. 141 (7) (1994) 1900–1904.
[11] C.-H. Yao, D. L. Feke, K. M. Robinson, S. Meikle, Contact mechanics and lubrication hydrodynamics of chemical mechanical polishing, J. Electrochem. Soc. 147 (4) (2000) 1502–1512.
[12] D. Arbelaez, T. I. Zohdi, D. A. Dornfeld, Modeling and simulation of material removal with particulate flows, Comput. Mech. 42 (5) (2008) 749–759.

[13] C. Zhou, L. Shan, J. R. Hight, S. H. Ng, S. Danyluk, Fluid pressure and its effects on chemical mechanical polishing, Wear 253 (2002) 430–437.
[14] N. Mueller, C. Rogers, V. P. Manno, R. White, M. Moinpour, In situ investigation of slurry flow fields during CMP, J. Electrochem. Soc. 156 (12) (2009) H908–H912.
[15] D. Zhao, Y. He, X. Lu, In situ measurement of fluid pressure at the wafer-pad interface during chemical mechanical polishing of 12-inch wafer, J. Electrochem. Soc. 159 (1) (2012) H22–H28.
[16] E. J. Terrell, C. F. Higgs III, Hydrodynamics of slurry flow in chemical mechanical polishing, J. Electrochem. Soc. 153 (6) (2006) K15–K22.
[17] S.-S. Park, C.-H. Cho, Y. Ahn, Hydrodynamic analysis of chemical mechanical polishing process, Tribol. Int. 33 (2000) 723–730.
[18] S. H. Ng, Measurement and Modeling of Fluid Pressures in Chemical Mechanical Polishing, Ph.D. thesis, Georgia Institute of Technology (2005).
[19] K. Cooper, J. Cooper, J. Groschopf, J. Flake, Y. Solomentsev, J. Farkas, Effects of particle concentration on chemical mechanical planarization, Electrochem. Solid State Lett. 5 (12) (2002) G109–G112.
[20] D. Tamboli, G. Banerjee, M. Waddell, Novel interpretations of CMP removal rate dependencies on slurry particle size and concentration, Electrochem. Solid State Lett. 7 (10) (2004) F62–F65.
[21] Z. Zhang, W. Liu, Z. Song, Effect of abrasive particle concentration on preliminary chemical mechanical polishing of glass substrate, Microelectron. Eng. 87 (2010) 2168–2172.
[22] E. Paul, A model of chemical mechanical polishing, J. Electrochem. Soc. 148 (6) (2001) G355–G358.
[23] Y.-R. Jeng, P.-Y. Huang, A material removal rate model considering interfacial micro-contact wear behaviour for chemical mechanical polishing, J. Tribol.-Trans. ASME 127 (2005) 190–197.
[24] Y. Wang, Y. Zhao, W. An, Z. Ni, J. Wang, Modeling effects of abrasive particle size and concentration on material removal at molecular scale in chemical mechanical polishing, Appl. Surf. Sci. 257 (2010) 249–253.
[25] Y. Y. Ye, R. Biswas, J. R. Morris, A. Bastawros, A. Chandra, Molecular dynamics simulation of nanoscale machining of copper, Nanotechnology 14 (10) (2003) 390–396.
[26] E. Chagarov, J. B. Adams, Molecular dynamics simulations of mechanical deformation of amorphous silicon dioxide during chemical-mechanical polishing, J. Appl. Phys. 94 (6) (2003) 3853–3861.
[27] P. M. Agrawal, L. M. Raff, S. Bukkapatnam, R. Komanduri, Molecular dynamics investigations on polishing of a silicon wafer with a diamond abrasive, Appl. Phys. A-Mater. Sci. Process. 100 (1) (2010) 89–104.
[28] L. B. Lucy, A numerical approach to the testing of the fission hypothesis, Astron. J. 82 (12) (1977) 1013–1024.
[29] R. A. Gingold, J. J. Monaghan, Smoothed particle hydrodynamics: Theory and application to non-spherical stars, Mon. Not. Roy. Astron. Soc. 181 (1977) 375–389.
[30] J. J. Monaghan, Smoothed particle hydrodynamics and its diverse applications, Annu. Rev. Fluid Mech. 44 (1) (2012) 323–346.
[31] K. Takano, K. Yamada, N. Takezawa, T. Suzuki, T. Inamura, SPH-based flow simulation of polishing slurry including polished debris in CMP, J. Jpn. Soc. Precis. Eng. 73 (1) (2007) 90–95, in Japanese.
[32] S. Adami, X. Y. Hu, N. A. Adams, A generalized wall boundary condition for smoothed

particle hydrodynamics, J. Comput. Phys. 231 (2012) 7057–7075.
[33] D. Wang, Y. S. Zhou, S. H. Shao, Effcient implementation of smoothed particle hydrodynamics (SPH) with plane sweep algorithm, preprint (2013).
[34] G. R. Liu, M. B. Liu, Smoothed Particle Hydrodynamics: A Meshfree Particle Method, World Scientific Publishing Co. Pte. Ltd., Singapore, 2003.
[35] W. Dehnen, H. Aly, Improving convergence in smoothed particle hydrodynamics simulations without pairing instability, Mon. Not. Roy. Astron. Soc. 425 (2) (2012) 1068–1082.
[36] J. P. Morris, P. J. Fox, Y. Zhu, Modeling low Reynolds number incompressible flows using SPH, J. Comput. Phys. 136 (1997) 214–226.
[37] J. J. Monaghan, Smoothed particle hydrodynamics, Rep. Prog. Phys. 68 (8) (2005) 1703–1759.
[38] D. J. Price, Smoothed particle hydrodynamics and magnetohydrodynamics, J. Comput. Phys. 231 (2012) 759–794.
[39] X. Y. Hu, N. A. Adams, A multi-phase SPH method for macroscopic and mesoscopic flows, J. Comput. Phys. 213 (2006) 844–861.
[40] S. Marrone, M. Antuono, A. Colagrossi, G. Colicchio, D. Le Touzé, G. Grazianni, δ-SPH model for simulating violent impact flows, Comput. Methods Appl. Mech. Engrg. 200 (2011) 1526–1542.
[41] J. J. Monaghan, Simulating free surface flows with SPH, J. Comput. Phys. 110 (1994) 399–406.
[42] G. K. Batchelor, An Introduction to Fluid Dynamics, Cambridge University Press, Cambridge, 1967.
[43] J. J. Monaghan, SPH without a tensile instability, J. Comput. Phys. 159 (2) (2000) 290–311.
[44] S. Adami, X. Y. Hu, N. A. Adams, A transport-velocity formulation for smoothed particle hydrodynamics, J. Comput. Phys. 241 (2013) 292–307.
[45] D. Molteni, A. Colagrossi, A simple procedure to improve the pressure evaluation in hydrodynamic context using the SPH, Comput. Phys. Commun. 180 (6) (2009) 861–872.
[46] J. Bonet, T.-S. Lok, Variational and momentum preservation aspects of smooth particle hydrodynamic formulations, Comput. Methods Appl. Mech. Engrg. 180 (1999) 97–115.
[47] J. Lu, C. Rogers, V. P. Manno, A. Philipossian, S. Anjur, M. Moinpour, Measurements of slurry film thickness and wafer drag during CMP, J. Electrochem. Soc. 151 (4) (2004) G241–G247.
[48] W. Lortz, F. Menzel, R. Brandes, F. Klaessig, T. Knothe, T. Shibasaki, News from the M in CMP-viscosity of CMP slurries, a constant?, MRS Proc. 767 (2003) 47–56.
[49] X.-J. Fan, R. I. Tanner, R. Zheng, Smoothed particle hydrodynamics simulation of non-Newtonian moulding flow, J. Non-Newton. Fluid Mech. 165 (2010) 219–226.
[50] J. J. Monaghan, A. Kos, N. Issa, Fluid motion generated by impact, J. Waterw. Port Coast. Ocean Eng.-ASCE 129 (6) (2003) 250–260.
[51] B. Bouscasse, A. Colagrossi, S. Marrone, M. Antuono, Nonlinear water wave interaction with floating bodies in SPH, J. Fluids Struct. 42 (2013) 112–129.
[52] R. Glowinski, T. W. Pan, T. I. Hesla, D. D. Joseph, J. Périaux, A fictitious domain approach to the direct numerical simulation of incompressible viscous flow past moving rigid bodies: application to particulate flow, J. Comput. Phys. 169 (2001) 363–426.
[53] J. J. Monaghan, Particle methods for hydrodynamics, Comput. Phys. Rep. 3 (2) (1985) 71–124.
[54] L. Hernquist, N. Katz, TreeSPH: A unification of SPH with the hierarchical tree method, Astrophys. J. Suppl. Ser. 70 (1989) 419–446.
[55] R. Courant, K. Friedrichs, H. Lewy, On the partial difference equations of mathematical physics, IBM J. Res. Dev. 11 (2) (1967) 215–234.

[56] J. J. Monaghan, Smoothed particle hydrodynamics, Annu. Rev. Astron. Astrophys. 30 (1992) 543–574.
[57] F. B. Kaufman, D. B. Thompson, R. E. Broadie, M. A. Jaso, W. L. Guthrie, D. J. Pearson, M. B. Small, Chemical-mechanical polishing for fabricating patterned W metal features as chip interconnects, J. Electrochem. Soc. 138 (11) (1991) 3460–3465.
[58] Y. Zhao, L. Chang, S. H. Kim, A mathematical model for chemical-mechanical polishing based on formation and removal of weakly bonded molecular species, Wear 254 (2003) 332–339.
[59] L. Chang, On the CMP material removal at the molecular scale, J. Tribol.-Trans. ASME 129 (2) (2007) 436–437.
[60] H. Hocheng, H. Y. Tsai, Y. T. Su, Modeling and experimental analysis of the material removal rate in the chemical mechanical planarization of dielectric films and bare silicon wafers, J. Electrochem. Soc. 148 (10) (2001) G581–G586.
[61] J. Xin, W. Cai, J. A. Tichy, A fundamental model proposed for material removal in chemical-mechanical polishing, Wear 268 (2010) 837–844.
[62] C. Feng, C. Yan, J. Tao, X. Zeng, W. Cai, A contact-mechanics-based model for general rough pads in chemical mechanical polishing processes, J. Electrochem. Soc. 156 (7) (2009) H601–H611.
[63] C. Antoci, M. Gallati, S. Sibilla, Numerical simulation of fluid-structure interaction by SPH, Comput. Struct. 85 (2007) 879–890.
[64] B. J. Hamrock, S. R. Schmid, B. O. Jacobson, Fundamentals of Fluid Film Lubrication, 2nd Edition, Marcel Dekker, Inc., New York, USA, 2004.
[65] A. F. Fortes, D. D. Joseph, T. S. Lundgren, Nonlinear mechanics of fluidization of beds of spherical particles, J. Fluid Mech. 177 (1987) 467–483.
[66] H. H. Hu, D. D. Joseph, M. J. Crochet, Direct simulation of fluid particle motions, Theor. Comput. Fluid Dyn. 3 (1992) 285–306.
[67] Z.-G. Feng, E. E. Michaelides, The immersed boundary-lattice Boltzmann method for solving fluid-particles interaction problems, J. Comput. Phys. 195 (2004) 602–628.
[68] M. Uhlmann, An immersed boundary method with direct forcing for the simulation of particulate flows, J. Comput. Phys. 209 (2005) 448–476.
[69] K. Qin, Multi-scale Modeling of the Slurry Flow and the Material Removal in Chemical Mechanical Polishing, Ph.D. thesis, The University of Florida (2003).
[70] R. D. White, A. J. Mueller, M. Shin, D. Gauthier, V. P. Manno, C. B. Rogers, Measurement of microscale shear forces during chemical mechanical planarization, J. Electrochem. Soc. 158 (10) (2011) H1041–H1051.
[71] F. Ilie, Models of nanoparticles movement, collision, and friction in chemical mechanical polishing (CMP), J. Nanopart. Res. 14 (3) (2012) 752.
[72] R. K. Singh, S.-M. Lee, K.-S. Choi, G. Bahar Basim, W. Choi, Z. Chen, B. M. Moudgil, Fundamentals of slurry design for CMP of metal and dielectric materials, MRS Bull. 27 (10) (2002) 752–760.